



Irradiation Direction-Dependent Surface Charge Recombination in Hematite Thin-Film Oxygen Evolution Photoanodes

Guancai Xie^{+, [a, b]} Xiaoyue Zhang^{+, [c]} Xiao Ouyang^{+, [a, b]} Qi Xin,^[a] Beidou Guo,^{*, [a, b]} and Jian Ru Gong^{*, [a]}

For photoelectrochemical (PEC) devices, light irradiation direction changes photogenerated charge distribution and thus will affect the charge collection efficiency of the photoelectrodes. Herein, we studied the influence of irradiation direction on charge collection properties of α -Fe₂O₃ photoanodes with different geometries, and demonstrated the controlled charge collection by modifying surface geometry. An irradiation direction-dependent surface charge recombination was identified. In comparison with backside irradiation, frontside irradiation

was found to be favorable to obtain high photocurrent because of the effective hole collection, except for the thick planar film due to its high surface recombination. This problem can be solved by patterning the planar film surface with nanonet geometry to promote surface charge transfer. As a result, the nanonet photoanode exhibited a higher photocurrent than the planar counterpart under frontside irradiation. Our finding provides useful guidance on designing high efficiency PEC devices.

Introduction

Photoelectrochemical (PEC) water splitting using semiconductors is a promising way to produce sustainable hydrogen fuel from solar energy.^[1–4] Since the pioneering work of the TiO₂ photoanode for PEC water splitting by Fujishima and Honda in 1972,^[5] plenty of semiconductors have been reported to be active for PEC water splitting, including n-type semiconductors like α -Fe₂O₃,^[6,7] BiVO₄,^[8] g-C₃N₄,^[9] and WO₃,^[10] as photoanodes for oxygen evolution and p-type semiconductors like Cu₂O^[11] as photocathodes for hydrogen evolution. To improve the PEC performance of semiconductor photoelectrodes, many strategies such as hetero atom doping,^[12] construction of heterostructures,^[13–15] and deposition of electrocatalysts,^[16–18] have been proposed. Overall, the key to optimizing the PEC cell lies in efficient collection of charge carriers generated in the

semiconductor photoelectrode under irradiation both at the semiconductor/substrate interface (SSI) and at the semiconductor/liquid junction (SCLJ).^[19,20] Studying the relevant kinetic processes of charge carriers is thus essential in the design and optimization of a PEC cell.


Light irradiation direction has found to affect charge collection properties because the light intensity distribution and hence the charge distribution in the photoelectrode will be changed under different light irradiation directions.^[21–23] There are two incident directions in PEC measurements, namely, the frontside irradiation (FI) and backside irradiation (BI). The former refers to light irradiation from the SCLJ side while the later the SSI side. It is generally believed that for photoanodes, FI is an electron transport limited condition and beneficial for hole collection because most of the photogenerated electrons need to diffuse through the film to the SSI for collection while BI is a hole transport limited condition and beneficial for electron collection.^[24,25] Xiao et al. identified a trap-limited electron transport region existing under BI in mesoporous BiVO₄ photoanodes, which leads to the higher PEC performance of BiVO₄ film under FI than that under BI.^[26] For a certain semiconductor photoelectrode, the preferable direction of irradiation depends on its electron and hole mobility.^[24] For example, undoped BiVO₄ nanoparticle photoanode has higher PEC activity under BI than FI due to its low electron mobility.^[25,27] Enhancing the electron transport property by doping can give identical or higher PEC activity under FI than BI, as observed in hydrogen-doped or Mo-doped BiVO₄ nanoparticles.^[8,28] The introduction of nanostructures can also affect the preferable irradiation direction on the material. Some nanostructured α -Fe₂O₃ photoanodes, such as mesostructured morphology^[16] or cauliflower,^[29] are commonly tested under FI for the larger photocurrent density than under BI. While some nanostructured α -Fe₂O₃ photoanodes, like the nanorods^[30] or nanoplate arrays^[31] show


[a] G. Xie,⁺ X. Ouyang,⁺ Prof. Q. Xin, B. Guo, Prof. J. R. Gong
Chinese Academy of Sciences (CAS)
Key Laboratory of Nanosystem and Hierarchy Fabrication
CAS Center for Excellence in Nanoscience
National Center for Nanoscience and Technology
Beijing 100190 (P. R. China)
E-mail: guobd@nanoctr.cn
gongjr@nanoctr.cn

[b] G. Xie,⁺ X. Ouyang,⁺ B. Guo
University of Chinese Academy of Sciences
Beijing 100049 (P. R. China)

[c] X. Zhang⁺
School of Materials and Energy
Southwest University
Chongqing 400715 (P. R. China)

[⁺] These authors contributed equally.

 Supporting information for this article is available on the WWW under <https://doi.org/10.1002/cctc.201901524>

 This manuscript is part of the Special Issue "Photocatalysis: From Solar Power to Sustainable Chemical Production", which is part of the wider project "Building A New Energy Economy with Catalysis".

high photocurrent only under BI. However, the comprehension of how the direction of irradiation affecting the carrier collection in semiconductor photoelectrodes with different geometries is still relatively limited.^[24,26]

Herein, taking hematite ($\alpha\text{-Fe}_2\text{O}_3$) photoanode as a model system, we investigated the influence of frontside irradiation and backside irradiation on charge collection property, by using a series of hematite photoelectrodes with different thicknesses and surface geometries. $\alpha\text{-Fe}_2\text{O}_3$ was chosen because it is a promising photoanode candidate owing to its low cost, environmentally benign, and earth-abundant nature, and especially due to an almost ideal energy bandgap (2.0–2.2 eV) and excellent chemical stability in a wide range of pH values.^[6,32–34] We found that, surface charge recombination property of the photoelectrode is closely related to the irradiation direction. Such irradiation direction-dependent surface recombination affects the charge collection efficiency and hence the PEC performance under different irradiation directions. FI is generally advantageous to get high photocurrent in hematite because of its effective photohole collection as compared to BI. However, due to the high recombination between photogenerated electrons and holes at the SCLJ, the thick planar $\alpha\text{-Fe}_2\text{O}_3$ photoanode shows a higher photocurrent under BI than that under FI at high applied biases. Specifically, we proposed a surface patterning method of patterning the planar film surface with nanonet geometry to tailor the charge collection property by suppressing the surface recombination via the promotion of interfacial charge transfer at the semiconductor-electrolyte interface, ultimately achieving a ten times photocurrent increase compared with the planar counterpart at 1.6 V under FI.

Results and Discussion

The hematite films were facily fabricated by thermal oxidation in air of thermal evaporated iron films on the substrates. By controlling the thickness of the evaporated iron film, we can obtain hematite films with different thicknesses. To investigate the influence of surface morphology on the charge collection property of the photoelectrode, two different substrates including bare indium tin oxide (ITO) and the ITO modified with a nanonet skeleton of hematite with a period of ca. 600 nm prepared by a sacrificial polystyrene template (see Figure S1) were used in this study, and the resultant photoanodes were named as Flat and Nanonet, respectively. Flat-25, Flat-100, Nanonet-25, and Nanonet-100 were prepared as representative samples, where the number indicates the thickness of the evaporated iron film.

Figure 1a–d shows scanning electron microscopy (SEM) images of the four photoanodes. For Flat samples, a coarse surface with hematite grains is observed in Flat-25 (Figure 1a), and the grains become coarser in the thick film (Figure 1b). This granular surface could be due to oxygen intake during the thermal oxidation process and the lower density of hematite compared to iron.^[35] For Nanonet samples, the resulting surface sustains the nanonet structure of the hematite skeleton in both

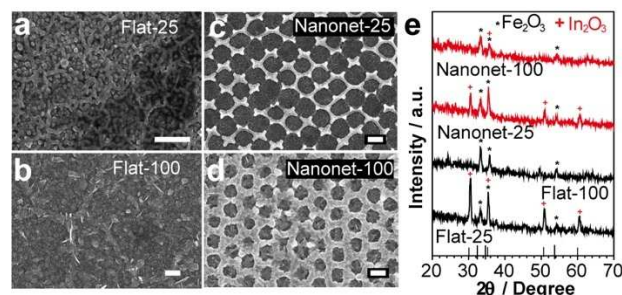


Figure 1. SEM images of (a) Flat-25, (b) Flat-100, (c) Nanonet-25, and (d) Nanonet-100 photoanodes; Scale bars are 500 nm. (e) The corresponding XRD patterns of the photoanodes.

thin and thick films. The X-ray diffraction (XRD) patterns of the four photoanodes are presented in Figure 1e. In all cases, characteristic peaks of $\alpha\text{-Fe}_2\text{O}_3$ at 33.1° , 35.6° and 54.1° are observed (PDF Card No. 00-033-0664), demonstrating the successful synthesis of $\alpha\text{-Fe}_2\text{O}_3$. Peaks appearing around 30.5° , 51.0° , and 60.5° can be attributed to In_2O_3 from the ITO substrate (PDF Card No. 03-065-31700). Absence of XRD peaks corresponding to metallic Fe also indicates the full oxidation of Fe film in all the photoanodes. UV-vis absorption spectra show that thick films have more light absorption than thin films for both Flat and Nanonet samples regardless of the irradiation direction due to the increased optical path length in thick films (Figure S2). Moreover, the irradiation direction has little effect on the light absorption of the Flat-25 sample, but for the Flat-100 and Nanonet samples (Nanonet-25 and Nanonet-100), BI can give higher light absorption in the hematite films than FI. Besides, by comparing the Flat samples with the Nanonet samples with the same thickness, we found that under BI the Flat and the Nanonet samples have the similar light absorption while under FI the Nanonet samples have smaller light absorption than the Flat ones.

The effect of the irradiation direction on the PEC performance of the four photoanodes with different thicknesses and surface geometries was evaluated by photocurrent density-applied potential (J – V) plots. As can be seen in Figure 2, the photocurrent density of the photoanodes under frontside and backside irradiation is related not only to the film thickness but also to the film geometry. The photocurrent density under FI is typically larger than the photocurrent density under BI for the same photoanode except for the Flat-100 sample where the FI photocurrent is overtook by the BI photocurrent when the applied bias is higher than 1.4 V versus reverse hydrogen electrode (V_{RHE}). Light absorption can be excluded here as the main factor causing the above observations due to the fact that BI typically gives higher light absorption in the hematite films than FI. As widely known, hematite has a very small hole diffusion length of 2–4 nm,^[36] and thus FI is prefer to get a high photocurrent density due to the favorable photohole collection.^[24] The abnormal phenomenon in Flat-100 suggests that the photohole collection becomes inefficient at high biases under FI, and the reason will be discussed later. To fully exert the advantage of one certain irradiation direction for practical

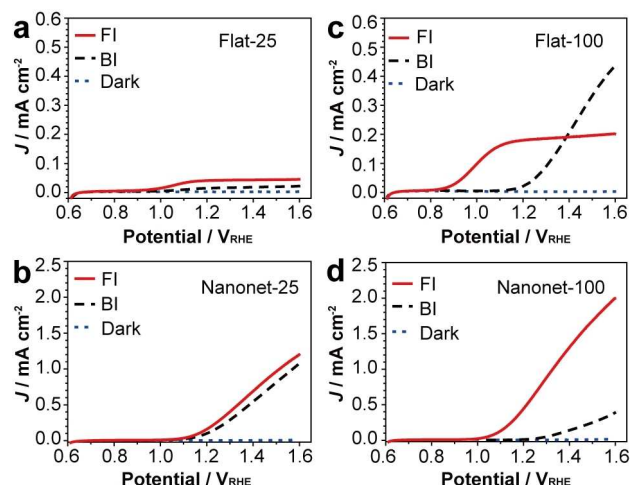


Figure 2. J–V curves in the dark, under backside irradiation and frontside irradiation of: (a) Flat-25, (b) Flat-100, (c) Nanonet-25, and (d) Nanonet-100.

application, such abnormal phenomenon that FI photocurrent is overtook by BI photocurrent at large bias range should be avoided, which can be realized by patterning the planar surface with nanonet structure as demonstrated in Nanonet-100. In addition, Figure 2 shows that under FI the thick hematite photoanodes (Flat-100 and Nanonet-100) always show higher photocurrents than the thin hematite photoanodes (Flat-25 and Nanonet-25), which can be attributed to the enhanced light absorption in thick hematite films. Most importantly, under FI the Nanonet-100 photoanode can give a higher photocurrent at 1.23 V_{RHE} as compared to the Flat-100 photoanode.

The charge separation efficiency (η_{sep}) and charge injection efficiency (η_{inj}) were thus measured to investigate the effect of irradiation directions on the charge collection property of the photoanodes with different thicknesses and geometries. In all cases, as shown in in Figure 3, the charge separation efficiencies are all very low (typically lower than 20%) due to the inferior conductivity of hematite. Interestingly, η_{inj} of each photoanode exhibits similar shape with their corresponding J–V curves, and the relative relationship of η_{inj} under different irradiation directions is also consistent with that of their corresponding photocurrent density. Especially, in the Flat-100 photoanode, η_{inj} under FI is also overtook by that under BI at applied biases larger than 1.4 V_{RHE} . These observations suggest that the charge collection property of the photoanodes also depends on the film thickness and geometry and the PEC activity is mainly determined by the hole collection efficiency of the photoanode. Furthermore, by comparing η_{inj} of photoanodes with the same thickness, it can be deduced that the nanonet surface can help to improve hole collection under FI.

The interfacial charge transport at the SCLJ is the key causing the difference on hole collection efficiency under different irradiation directions, which depends on the film thickness and especially geometry. As thin hematite films with both Flat and Nanonet surface geometries show very low photocurrent density due to their insufficient light absorption,

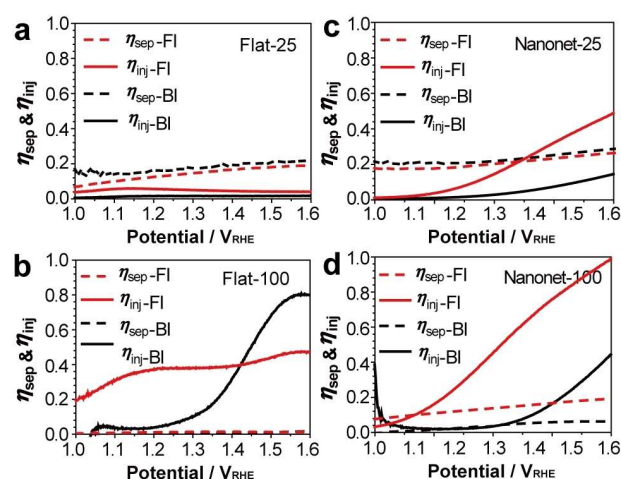


Figure 3. Charge injection efficiency (η_{inj}) and charge separation efficiency (η_{sep}) of (a) Flat-25, (b) Flat-100, (c) Nanonet-25, and (d) Nanonet-100 under frontside irradiation and backside irradiation.

we will mainly discuss on thick films hereafter. To investigate the difference of such interfacial charge transfer, transient photocurrent under different bias was recorded. In photoanodes, an anodic photocurrent spike is generated during the switching of the electrode from a dark state to a light, corresponding to the equilibrium process in which photo-generated holes accumulate at the SCLJ and gradually recombine with photogenerated electrons (Figure S4).^[37–39] Figure 4a displays that in comparison with that under FI the decay of anodic photocurrent spikes of Flat-100 at high bias potential, especially greater than 1.5 V_{RHE} , becomes slow under BI, which suggests the strong surface recombination of photogenerated electrons and holes in planner hematite due to the great electron flow in the space charge layer under FI.^[40] Therefore, we can conclude that severe charge recombination at the SCLJ under FI may contribute to the low hole collection at high biases in the Flat-100 sample. In contrast, the anodic photocurrent spike of Nanonet-100 under FI is almost invisible when the applied bias is larger than 1.3 V_{RHE} (Figure 4b), indicating that the nanonet structure can effectively suppress the recombination of photogenerated electrons and holes at the SCLJ.

Photoelectrochemical impedance spectra (PEIS) were attained to further reveal the charge transfer property at the SCLJ as well as in the bulk photoanodes. The equivalent circuit used for PEIS data fitting is shown in Figure S5, where R_{series} represents the series resistance, R_{SC} and R_{CT} represent for charge transfer resistance in the bulk photoanode and at the semiconductor/electrolyte interface, and C_{H} and C_{SC} represent the capacitance of the Helmholtz layer and of the space charge layer, respectively. By comprising R_{SC} between FI and BI, we found that Flat-100 exhibits a much larger R_{SC} under FI at high biases (Figure 5a), implying that the collection of electrons is hindered in its bulk under FI at high biases; In contrast, the R_{SC} of Nanonet-100 under FI becomes small at high biases and no dramatic rise like that in Flat-100 observed (Figure 5b), indicat-

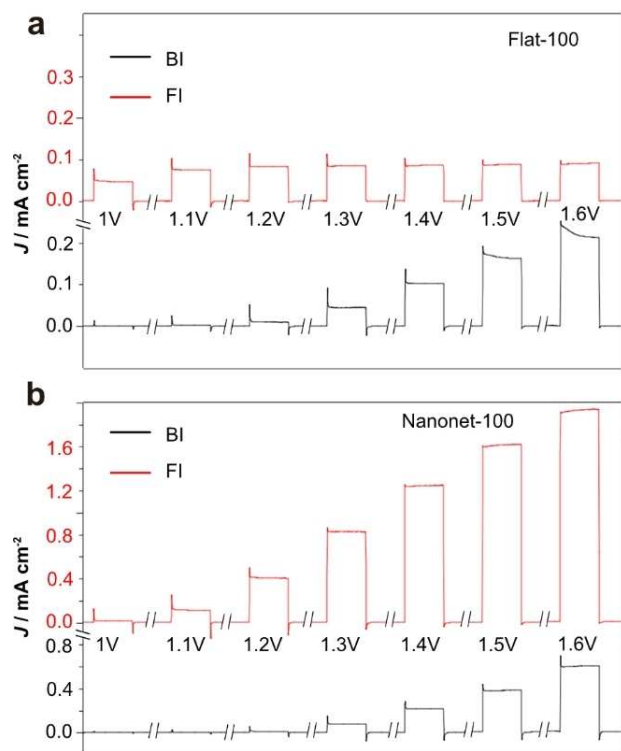


Figure 4. Transient photocurrent of (a) Flat-100 and (b) Nanonet-100 at different bias voltages under both frontside irradiation and backside irradiation.

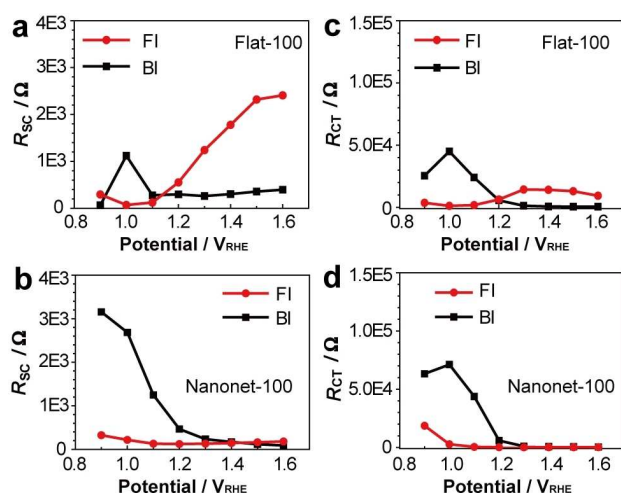
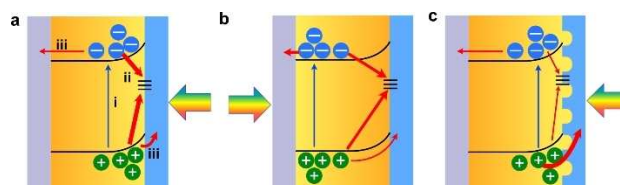


Figure 5. The R_{sc} under frontside irradiation and backside irradiation: (a) Flat-100, (b) Nanonet-100; The R_{ct} under frontside irradiation and backside irradiation: (c) Flat-100, (d) Nanonet-100.

ing the electron suppressed in the bulk has been relieved in nanonet structure. Moreover, it can be observed from Figure 5c that for the Flat-100 sample, R_{ct} under FI becomes larger with increasing the applied biases and finally exceeds the values under BI, validating its high surface charge recombination at the SCLJ at high applied biases. For the Nanonet-100 sample, in

contrast, R_{ct} is found to be small in the entire bias range under FI and is also smaller than that under BI (Figure 5d), which confirms that the nanonet structure can effectively promote the interfacial charge transfer at the SCLJ especially under FI, which may be due to the high surface area and the increased ratio of built-in electric filed.^[9] More information for R_{sc} and R_{ct} of Nanonet-25 can be found in Figure S6 and S7, which show similar results with Nanonet-100.

Based on above experimental observations, we present in Scheme 1 a proposed scheme of charge transfer behavior under frontside and backside irradiation. The generation rate of photogenerated carriers is positively correlated with the light intensity: photogenerated electrons and holes will mainly distribute at the SCLJ under FI and will mainly distribute close to the SSI under BI.^[41] For both the Flat-100 and Nanonet-100 samples, the photocurrent density measured in the electrolyte with the H_2O_2 hole sacrificial agent under FI is always greater than that under BI, demonstrating that more photogenerated holes can actually transfer across the SCLJ (Figure S8). However, the electrons need to diffuse across the film to the collection substrate, thus resulting in an increase in the recombination of electrons and holes within the bulk as well as at the SCLJ under FI (Scheme 1a). As for the case of BI (Scheme 1b), most of the photogenerated electrons can be effectively collected by the ITO substrate within the collection distance. Although the holes have to travel across the film before injection, the increased width of the depletion layer under high biases^[42,43] will hinder the diffusion of electrons to the SCLJ and hence suppress their recombination with holes at the SCLJ. Simultaneously, the increased surface band bending at high biases will increase the surface hole concentration, which is beneficial to interfacial charge transfer.^[44] Taken together, the injection efficiency under BI will increase remarkably when the bias voltage is high. In contrary, under FI, the accumulated holes near the photoanode surface at high biases due to the increased surface bend bending can easily and fast recombine with the high surface electron concentration (Scheme 1a). As a result, the hole collection (i.e., injection rate of holes) under FI becomes lower than that under BI at high biases as in the case of thick film. The above mechanism also suggests that the bias at which the BI photocurrent overtakes the FI photocurrent will shift positively with decreasing the film thickness due to the fact that the backside photoelectrons under BI will become more



Scheme 1. Mechanism of charge generation (i), surface recombination (ii), and transport (iii) processes in (a) Flat under FI, (b) Flat under BI, and (c) Nanonet under FI. The gray, orange, and blue section denote ITO substrate, hematite film, and electrolyte, respectively. Solid blue arrows signify the charge generation. Solid red arrows highlight charge recombination and transfer processes. The thickness of the arrows signifies their relative impact in the above-mentioned processes.

easily to recombine with surface photoholes in thin films at a certain bias. This is further demonstrated in the Flat-50 sample, and its FI photocurrent is overtaken by the BI photocurrent at an applied bias of ca. $1.45 V_{RHE}$, which is higher than that in the Flat-100 sample (Figure S9). Patterning the surface with nanonet structure helps to suppress the surface recombination between photogenerated electrons and holes in both thin and thick films. As shown in Scheme 1c, under FI, the nanonet structure can enhance the injection of holes at the SCLJ due to the high surface area and the increased ratio of built-in electric field, which decreases the surface photohole concentration and thus reduce their recombination with electrons. The above conclusions are further supported by observations in the Flat-50 sample (Figure S10–S12).

Although the onset potential of nanonet samples is a little higher than flat ones, there is a significant improvement on PEC activity for nanonet-structured films under FI: the photocurrent of the Flat-100 sample is only 0.2 mA cm^{-2} at a bias voltage of $1.6 V_{RHE}$; while at the same bias voltage, the Nanonet-100 sample has a photocurrent of approximately 2 mA cm^{-2} , achieving ten times performance increase compared with the planar hematite. This PEC enhancement under FI is mainly explained as follows: i) Shorter charge collection distance. In the case of a planar hematite photoanode, hole diffusion length is shorter relative to the light penetration depth, and consequently, most of the photogenerated holes cannot diffuse to the surface of the photoelectrode to inject into the electrolyte. For the nanonet hematite electrode, the distance from the location where the holes are generated to the SCLJ is much shorter than that of a planar hematite electrode. It is thus expected that bulk recombination is greatly reduced in the nanonet hematite electrode. ii) Larger surface area. The nanonet electrode also possesses a larger surface area contacted with the electrolyte, which implies that the nanonet film has a larger space charge region with respect to the flat film. The increased space charge region can significantly enhance the separation of the photogenerated charge carriers, and consequently, the charge carrier recombination can be suppressed.

Conclusions

In summary, we investigated the influence of irradiation direction on charge collection property of $\alpha\text{-Fe}_2\text{O}_3$ with different thicknesses and surface geometries and identified the irradiation direction-dependent surface charge recombination property in $\alpha\text{-Fe}_2\text{O}_3$. We demonstrated that for planar geometry, the frontside irradiation is beneficial to photohole collection at the SCLJ, but it is not conducive to the transmission of photogenerated electrons in the bulk, thus resulting in severe surface recombination in thick planar films at high bias. Patterning the planar surface with nanonet geometry can not only further enhance the transfer of holes at the SCLJ due to the high surface area and increased ratio of built-in electric field, but also suppress surface recombination under frontside irradiation. As a result, a ten-time significant improvement on the PEC activity at $1.6 V_{RHE}$ was achieved under frontside irradiation for the nano-

net-structured hematite as compared to the planar-structured hematite. We believe our work will provide useful guidelines for the design of PEC devices with high efficiencies.

Experimental Section

Synthesis of planar hematite photoanodes. First, Fe thin films with different thicknesses of 25 and 100 nm were deposited on an indium tin oxide (ITO)-coated glass substrate by thermal evaporating metallic Fe particles (ZhongNuo New Materials) with a rate of 0.3 to 0.4 Å/s using a high vacuum resistance evaporation coating machine (ZHD-300), and the film thickness was controlled using quartz crystal thickness monitor. Then, the Fe film was annealed at 450°C for 1 hour with a ramp-up rate of 5°C/min in a Muffle Furnace (KXL-1100X). After natural cooling, planar hematite photoanodes were obtained.

Synthesis of hematite photoanodes with nanonet surface structure. A polystyrene microsphere template with a diameter of 600 nm was first prepared on ITO according to previous report (see Supplemental Note 1 in Supporting Information).^[45] A mixed solution of $\text{FeCl}_3 \cdot 6\text{H}_2\text{O}$ and citric acid both having a concentration of 0.06 M was prepared, with ethanol as the solvent, magnetically stirring until completely dissolved. A sufficient amount of the precursor solution was taken up using a 5 ml syringe, and a drop of the solution was dropped at the center of the ITO covered with a single-layer polystyrene microsphere. Waiting for 30–60 s, place it in a Muffle Furnace for heat treatment in air atmosphere. The films were kept at 110°C for 2 h, and then annealed at 450°C for 3 h with a ramp-up rate of 0.5°C/min . After natural cooling, we got the $\alpha\text{-Fe}_2\text{O}_3$ nanonet skeleton.^[46–47] Subsequently, Fe films with thickness of 25 nm and 100 nm were deposited on the nanonet skeleton by thermal evaporation, with same evaporation rate and annealing condition as preparing planar hematite films. In this way, we obtained hematite photoanode with surface patterning of nanonet structure.

Material Characterization. The crystalline phase structures of the prepared planar $\alpha\text{-Fe}_2\text{O}_3$ and nanonet $\alpha\text{-Fe}_2\text{O}_3$ samples were determined by X-ray diffraction (X'Pert PRO MPD) with Cu K α radiation over the 2θ range of 20° – 80° . The scanning electron microscopy (SEM) was conducted to obtain the thickness and surface morphology, which was analyzed using a Hitachi S-4800 Field-emission scanning electron microscope operated at 10 kV. The ultraviolet-visible (UV-Vis) transmittance and reflectance spectra were obtained using a UV-vis spectrophotometer (UV-2600) equipped with an external diffuse reflectance accessory (DRA-2500), and the absorbance (A) was calculated by the formula $A = 1 - T - R$, where T is the total transmittance and R is the total reflectance.

Photoelectrochemical Measurements. All of the photoelectrochemical measurements were carried out in an electrochemical workstation (Zahner Zennium, Germany) in a typical three-electrode configuration with the prepared photoanode as the working electrode, a Pt foil as the counter electrode, a saturated Ag/AgCl electrode as the reference electrode, and 1 M NaOH (pH = 13.6) aqueous solution as the electrolyte. The samples with the geometrical area of 0.636 cm^2 were illuminated with a 150 W xenon lamp (CT-XE-150) and the light intensity was measured to be $\sim 500 \text{ mW cm}^{-2}$. The photocurrent density-applied potential (J–V) plots of the photoanodes were scanned at 20 mV s^{-1} between -400 mV and 700 mV vs. the saturated Ag/AgCl electrode. Photoelectrochemical impedance spectra (PEIS) were recorded under light irradiation condition at frequencies from 100000 to 0.1 Hz with a sinusoidal potential perturbation of 10 mV. EIS data were fitted according to a classical equivalent circuit model using

ZSimpWin software. All the measured potentials against the saturated Ag/AgCl electrode were converted to the reversible hydrogen electrode (RHE) scale according to the Nernst Equation [Eq. (1)]:

$$E_{\text{RHE}} = E_{\text{Ag/AgCl}} + 0.059 \times \text{pH} + E_{\text{Ag/AgCl}}^0 \quad (1)$$

Wherein E_{RHE} is the converted potential vs. RHE, $E_{\text{Ag/AgCl}}$ is the measured potential against the saturated Ag/AgCl electrode, and $E_{\text{Ag/AgCl}}^0$ is the standard potential of the saturated Ag/AgCl electrode (0.197 V at 25°C).

Calculation of Charge Separation and Injection Efficiencies. The charge separation efficiency (η_{sep}) represents the yield of the photogenerated holes that reach the SCLJ without bulk recombination. The charge injection efficiency (η_{inj}) describes the output of the photogenerated holes that are successfully injected into the electrolyte to trigger water oxidation without recombining with the electrons at surface trap states. By assuming the charge injection efficiency to be 100% in the presence of the hole scavenger (H_2O_2) in the electrolyte, these two efficiencies were calculated using the Equations (2) and (3):

$$\eta_{\text{sep}} = J_{\text{H}_2\text{O}_2} / J_{\text{absorbed}} \quad (2)$$

$$\eta_{\text{inj}} = J_{\text{H}_2\text{O}} / J_{\text{H}_2\text{O}_2} \quad (3)$$

where $J_{\text{H}_2\text{O}_2}$ is the photocurrent density gained with the addition of the hole scavenger (0.5 M H_2O_2) to the 1 M NaOH solution, $J_{\text{H}_2\text{O}}$ is the water oxidation photocurrent density in 1 M NaOH solution, and J_{absorbed} is the photon absorption rate expressed as a current density, which can be calculated by using the Equation (4):

$$J_{\text{absorbed}} = \frac{e}{hc} \times \int_{\lambda_a}^{\lambda_b} P_{(\lambda)} A_{(\lambda)} \lambda d\lambda \quad (4)$$

where λ_a is the shortest wavelength of the light emitted by the light source; λ_b is the wavelength of the absorption edge of the photoelectrode; P , λ , h , c , e , and A are the power of incident photons, the wavelength of incident monochromatic light, the Planck constant, the speed of light, the elementary charge, and the absorbance of the photoelectrode, respectively.

Acknowledgements

The authors acknowledge financial support for this work from the National Natural Science Foundation of China (21422303, 21573049, 21872043, 81602643), National Key R&D Program "nanotechnology" special focus (2016YFA0201600), Beijing Natural Science Foundation (2142036), and the Knowledge Innovation Program, Youth Innovation Promotion Association, and Special Program of "One Belt One Road" of CAS.

Conflict of Interest

The authors declare no conflict of interest.

Keywords: Charge transfer • hematite • irradiation direction • nanonet structure • water splitting

- [1] M. Grätzel, *Nature* **2001**, 414, 338.
- [2] N. S. Lewis, *Science* **2007**, 315, 798–801.
- [3] J. H. Kim, D. Hansora, P. Sharma, J.-W. Jang, J. S. Lee, *Chem. Soc. Rev.* **2019**, 48, 1908–1971.
- [4] Y. He, T. Hamann, D. Wang, *Chem. Soc. Rev.* **2019**, 48, 2182–2215.
- [5] A. Fujishima, K. Honda, *Nature* **1972**, 238, 37–38.
- [6] K. Zhang, T. Dong, G. Xie, L. Guan, B. Guo, Q. Xiang, Y. Dai, L. Tian, A. Batool, S. U. Jan, R. Boddula, A. A. Thebo, J. R. Gong, *ACS Appl. Mater. Interfaces* **2017**, 9, 42723–42733.
- [7] W. Wang, B. Guo, H. Dai, C. Zhao, G. Xie, R. Ma, M. Z. Akram, H. Shan, C. Cai, Z. Fang, *Nano Lett.* **2019**, 19, 6133–6139.
- [8] J. K. Cooper, S. B. Scott, Y. Ling, J. Yang, S. Hao, Y. Li, F. M. Toma, M. Stutzmann, K. V. Lakshmi, I. D. Sharp, *Chem. Mater.* **2016**, 28, 5761–5771.
- [9] B. Guo, L. Tian, W. Xie, A. Batool, G. Xie, Q. Xiang, S. U. Jan, R. Boddula, J. R. Gong, *Nano Lett.* **2018**, 18, 5954–5960.
- [10] Y. Li, Z. Liu, J. Zhang, Z. Guo, Y. Xin, L. Zhao, *J. Alloys Compd.* **2019**, 790, 493–501.
- [11] D. Chen, Z. Liu, Z. Guo, W. Yan, Y. Xin, *J. Mater. Chem. A* **2018**, 6, 20393–20401.
- [12] D. Chen, Z. Liu, *ChemSusChem* **2018**, 11, 3438–3448.
- [13] Y. Lan, Z. Liu, Z. Guo, X. Li, L. Zhao, L. Zhan, M. Zhang, *Dalton Trans.* **2018**, 47, 12181–12187.
- [14] Z. Liu, Q. Song, M. Zhou, Z. Guo, J. Kang, H. Yan, *Chem. Eng. J.* **2019**, 374, 554–563.
- [15] Y. Abbas, Z. Zuhra, N. Akhtar, S. Ali, J. R. Gong, *ACS Appl. Energy Mater.* **2018**, 1, 3529–3536.
- [16] D. K. Zhong, D. R. Gamelin, *J. Am. Chem. Soc.* **2010**, 132, 4202–4207.
- [17] R. Boddula, B. Guo, A. Ali, G. Xie, Y. Dai, C. Zhao, Y. Wei, S. U. Jan, J. R. Gong, *ACS Appl. Energy Mater.* DOI: 10.1021/acsaem.9b01209.
- [18] B. Guo, A. Batool, G. Xie, R. Boddula, L. Tian, S. U. Jan, J. R. Gong, *Nano Lett.* **2018**, 18, 1516–1521.
- [19] G. Segev, H. Dotan, D. S. Ellis, Y. Piekner, D. Klotz, J. W. Beeman, J. K. Cooper, D. A. Grave, I. D. Sharp, A. Rothschild, *Joule* **2018**, 2, 210–224.
- [20] Z. Luo, T. Wang, J. Zhang, C. Li, H. Li, J. Gong, *Angew. Chem. Int. Ed.* **2017**, 56, 12878–12882; *Angew. Chem.* **2017**, 129, 13058–13062.
- [21] M. G. Walter, E. L. Warren, J. R. McKone, S. W. Boettcher, Q. Mi, E. A. Santori, N. S. Lewis, *Chem. Rev.* **2010**, 110, 6446–6473.
- [22] J. Reichman, *Appl. Phys. Lett.* **1980**, 36, 574–577.
- [23] D. E. Aspnes, *Surf. Sci.* **1983**, 132, 406–421.
- [24] W. Qiu, S. Xiao, Y. Tong, S. Yang, *J. Phys. Chem. C* **2019**, 123, 18753–18770.
- [25] Y. Liang, T. Tsubota, L. P. A. Mooij, R. V. D. Krol, *J. Phys. Chem. C* **2011**, 115, 17594–17598.
- [26] S. Xiao, H. Chen, Z. Yang, X. Long, Z. Wang, Z. Zhu, Y. Qu, S. Yang, *J. Phys. Chem. C* **2015**, 119, 23350–23357.
- [27] K. E. Kweon, G. S. Hwang, J. Kim, S. Kim, S. Kim, *Phys. Chem. Chem. Phys.* **2015**, 17, 256–260.
- [28] Y. Park, D. Kang, K.-S. Choi, *Phys. Chem. Chem. Phys.* **2014**, 16, 1238–1246.
- [29] I. Cesar, K. Sivula, A. Kay, R. Zboril, M. Grätzel, *J. Phys. Chem. C* **2009**, 113, 772–782.
- [30] N. Beermann, L. Vayssieres, S. E. Lindquist, A. Hagfeldt, *J. Electrochem. Soc.* **2000**, 147, 2456–2461.
- [31] J. Wang, J. Su, L. Guo, *Chem. Asian J.* **2016**, 11, 2328–2334.
- [32] K. Sivula, F. Le Formal, M. Grätzel, *ChemSusChem* **2011**, 4, 432–449.
- [33] S. Shen, S. A. Lindley, X. Chen, J. Z. Zhang, *Energy Environ. Sci.* **2016**, 9, 342–352.
- [34] C. Li, Z. Luo, T. Wang, J. Gong, *Adv. Mater.* **2018**, 30, 1707502.
- [35] P. Hiralal, S. Saremi-Yarahmadi, B. C. Bayer, H. Wang, S. Hofmann, K. U. Wijayantha, G. A. Amaratunga, *Sol. Energy Mater. Sol. Cells* **2011**, 95, 1819–1825.
- [36] D. A. Wheeler, G. Wang, Y. Ling, Y. Li, J. Z. Zhang, *Energy Environ. Sci.* **2012**, 5, 6682–6702.
- [37] F. L. Formal, N. Tétreault, M. Cornuz, T. Moehl, M. Grätzel, K. Sivula, *Chem. Sci.* **2011**, 2, 737–743.
- [38] S. R. Pendlebury, W. Xiuli, L. F. Florian, C. Maurin, K. Andreas, T. S. David, G. T. Michael, J. R. Durrant, *J. Am. Chem. Soc.* **2014**, 136, 9854–9857.
- [39] L. F. Florian, S. R. Pendlebury, C. Maurin, T. S. David, G. T. Michael, J. R. Durrant, *J. Am. Chem. Soc.* **2014**, 136, 2564–2574.
- [40] M. Mokhtarimehr, S. A. Tatarkova, *J. Opt. Soc. Am. B* **2017**, 34, 1705–1712.

- [41] Z. Zhang, J. T. Y. Jr, *Chem. Rev.* **2012**, *112*, 5520.
- [42] O. Hayden, G. Zheng, P. Agarwal, C. M. Lieber, *Small* **2007**, *3*, 2048–2052.
- [43] A. C. Twitchett, R. E. Dunin-Borkowski, P. A. Midgley, *Phys. Rev. Lett.* **2002**, *88*, 238302.
- [44] G. Xie, L. Guan, L. Zhang, B. Guo, A. Batool, Q. Xin, R. Boddula, S. U. Jan, J. R. Gong, *Nano Lett.* **2019**, *19*, 1234–1241.
- [45] M. Szekeres, O. Kamalin, P. Grobet, R. Schoonheydt, K. Wostyn, K. Clays, A. Persoons, I. Dekany, *Colloids Surf. A* **2003**, *227*, 77–83.
- [46] C. Hao, L. Hu, X. Fang, L. Wu, *Adv. Funct. Mater.* **2012**, *22*, 1229–1235.
- [47] Z. Zhang, K. Yu, B. Li, J. Zhu, H. Yin, L. Lou, Z. Zhu, *Appl. Phys. B* **2012**, *107*, 119–124.

Manuscript received: August 19, 2019
 Revised manuscript received: September 28, 2019
 Accepted manuscript online: September 30, 2019
 Version of record online: October 21, 2019
